ADVANCED FUNCTIONAL MATERIALS
www.afm-journal.de

www.MaterialsViews.com

Integrated Photo-supercapacitor Based on Bi-polar TiO_2 Nanotube Arrays with Selective One-Side Plasma-Assisted Hydrogenation

Jing Xu, Hui Wu, Linfeng Lu, Siu-Fung Leung, Di Chen, Xiaoyuan Chen, Zhiyong Fan, Guozhen Shen, and Dongdong Li**

One-dimensional anodic titanium oxide (ATO) nanotube arrays hold great potential as electrode materials for both dye-sensitized solar cells (DSSCs) and electrochemical supercapacitors (SCs). In this work, a novel stack-integrated photo-supercapacitor (PSC) thin-film device is presented, composed of a DSSC and a SC built on bi-polar ATO nanotube arrays, where an improved SC performance is achieved through selective plasma-assisted hydrogenation treatment. At a high current density of 1 mA/cm^2 in charge/discharge measurements, the areal capacitance of selective hydrogenated ATO two-electrode sub-device is substantially increased ~5.1 times, with the value as high as 1.100 mF/cm^2. The optimized PSC exhibits a remarkable overall photoelectric conversion and storage efficiency up to 1.64%, with fast response and superior cycling capability for more than 100 photocharge/galvanostatic discharge cycles without any decay. To meet applicable demands with a larger output voltage, a tandem PSC system is constructed, serving as the self-driven power source for an LED.

1. Introduction

Recent advances of sustainable energy conversion and storage technologies have led to continued improvements to meet future energy demands without increasing harmful emissions.[1,2] Dye sensitized solar cells (DSSCs), with the energy conversion efficiency up to 15%, are considered as one of the most promising candidates of the third generation photovoltaic cells.[1] Meanwhile, electrochemical supercapacitors (SCs) with superiorities of high power density, fast charge/discharge rate (in seconds) and stable cycling performance, have attained great research interest for the applications in hybrid electric vehicles, portable consumer electronics, and solar power plants, etc.[2]

Generally, the photo-energy conversion and energy storage devices are always operated independently, resulting in some space and energy consumption from the external connection system. Recently, much attempts have been made to integrate the energy conversion and storage devices into individual units for highly-efficient, light-weight and portable devices.[3–10] A photo-supercapacitor (PSC) has been designed by incorporating both organic photovoltaic and supercapacitor, leading to a 43% reduction in device internal resistance as compared to external wire connection.[11] Taking advantages of nanotechnologies, TiO_2 based integrated devices for both energy conversion and energy storage have been developed, such as the stacked photo-lithium battery and wire-like photo-supercapacitor.[6,7] However, the relatively poor conductivity hampers the prospects for practical applications.[7] Some efforts have been devoted to enhance the elelctrical conductiviey, including metal doping, non-metal doping and hydrogenation.[12–14] Comparing with the traditional hydrogen gas treatment method at high temperature, hydrogen plasma treatment has been demonstrated as a more efficient way to boost the capacitive performance of TiO_2 films in our previous work, exhibiting a high areal capacitance of 7.22 mF/cm^2 in a three-electrode configuration.[15] More importantly, the plasma technique provides the feasibility on selective treatment with the feature size down to micrometer scale.

In this paper, plasma-assisted hydrogenated anodic titanium oxide (ATO) nanotube films are systematically investigated for both DSSCs and SCs applications. The hydrogenation processes promote the capacitive performance of ATO based SC, while decrease the photoelectric conversion efficiency of the corresponding DSSC device. Subsequently, we propose a novel

J. Xu, Prof. G. Shen
State Key Laboratory for Superlattices and Microstructures, Institute of Semiconductors
Chinese Academy of Sciences
Beijing, 100083, China
E-mail: gzshen@semi.ac.cn
J. Xu, Prof. D. Chen
Wuhan National Laboratory for Optoelectronics (WNLO) and School of Optical and Electronic Information
Huazhong University of Science and Technology (HUST)
Wuhan, 430074, China
H. Wu, Dr. L. Lu, Prof. X. Chen, Prof. D. Li
Shanghai Advanced Research Institute
Chinese Academy of Sciences
Shanghai, 201210, China
E-mail: lidd@sari.ac.cn
S.-F. Leung, Prof. Z. Fan
Department of Electronic and Computer Engineering
Hong Kong University of Science and Technology
Hong Kong, China

DOI: 10.1002/adfm.201303042

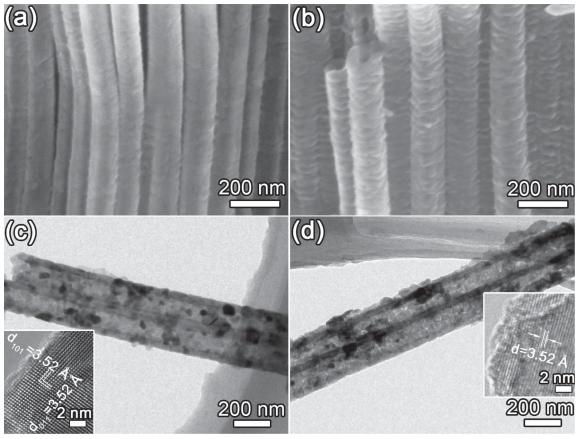

Figure 1. FESEM images of highly oriented (a) ATO and (b) ATO-H films. TEM images of (c) ATO and (d) ATO-H nanotubes. Insets in (c) and (d) show the corresponding HRTEM images.

stack-integrated PSC device composed of a DSSC and a SC built on bi-polar ATO nanotube arrays with selective hydrogen plasma treatment on SC side, which exhibits an outstanding overall photoelectric conversion and storage efficiency up to 1.64%. The integrated device shows fast response and superior cycling capability thanks to the selectivley improved electrical conductivity on SC side. As a demonstration, a series connected system with a maximum output voltage up to 2.5 V is constructed to drive a LED light.

2. Results and Discussion

2.1. Synthesis and Structural Analysis

Figure 1a and b present the field emission scanning electron microscopy (FESEM) images of TiO_2 nanotube arrays without (ATO) and with (ATO-H) hydrogen plasma treatment, respectively. Oriented nanotubes with diameters around 150 nm can still be observed in ATO-H films. Additionally, the side-wall of nanotubes presents highly rough surface after hydrogen plasma illumination. This unique structure is attributed to hydrogen plasma etching effect, which could further increase the electrode specific surface area.[16] Transmission electron microscopy (TEM) images for each sample are displayed in Figure 1c and d. High resolution TEM images in the corresponding insets indicate the anatase characteristic before and after plasma illumination.[17] Detailed analysis on crystal structure and chemical state can be found in our previous work.[15]

2.2. Integration of Photo-supercapacitor

2.2.1. DSSC Based on TiO_2 Arrays on Ti Foil

The electrochemical performances of both TiO_2 electrodes are subsequently characterized by assembling them into DSSC and symmetric SC devices. **Figure 2**a depicts *J–V* curves of back-side illuminated DSSCs based on ATO and ATO-H photoanodes,

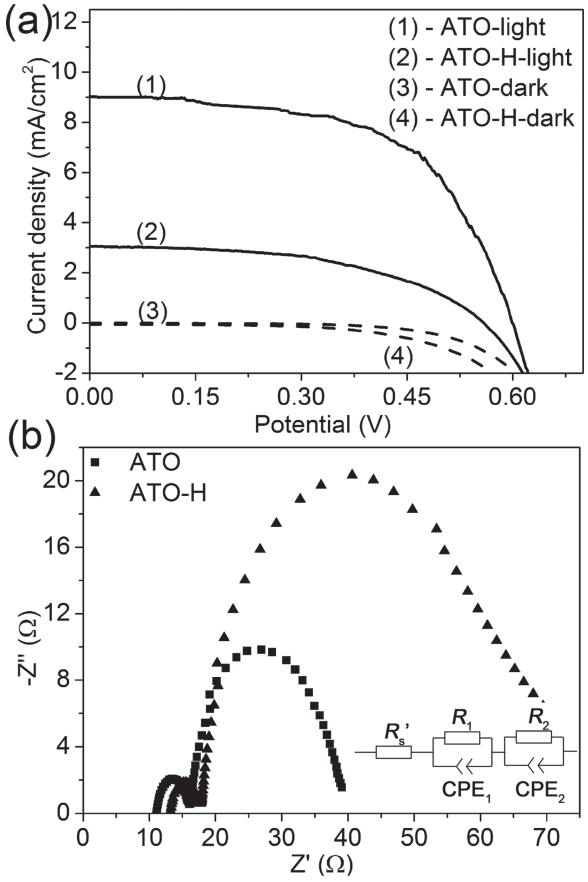

Figure 2. The *J–V* curves of the DSSCs with ATO and ATO-H photoanodes measured under simulated solar illumination (100 mW/cm^2). (b) Nyquist plots of the ATO DSSC and the ATO-H DSSC under dark condition. Inset of (b): Equivalent circuit for the Nyquist plots simulated by the Zsimpwin software.

respectively. The device, employing pristine ATO electrode, represents an overall power conversion efficiency (η_{DSSC}) of 3.17% with a short-circuit current density (J_{SC}) of 9.03 mA/cm^2, open circuit voltage (V_{OC}) of 0.63 V, and fill factor (*FF*) of 57.55%. As to the ATO-H based DSSC, a much lower J_{SC} of 3.07 mA/cm^2 with simultaniously depressed V_{OC} (0.56 V) and *FF* (49.48%) is obtained, yielding a much poorer efficiency of 0.85%. The shunt resistance (R_{sh}), approximated from the slope of the reverse *J–V* sweep at J_{SC}, is on the order of 1×10^3 Ω cm^2 for both devices. While equivalent series resistance (R_S) shows a distinct increase from 17.59 Ω cm^2 to 35.95 Ω cm^2, that can be estimated from the slopes of *J–V* curves at V_{oc}.[18]

Further insight into the DSSCs characteristics are conducted by electrochemical impedance spectroscopy (EIS) measurements at –0.7 V under dark conditions.[19] The Nyquist plots in Figure 2b display two semicircles, which can be simulated by the modeled equivalent circuit as illustrated in the inset of Figure 2b.[20,21] The modeled equivalent circuit composed of the sheet resistance of both substrates (R_S', intercept of the Nyquist plot with the *x*-axis), charge transport resistance at the counter electrode/electrolyte interface (R_1, first semicircle in the plot) and at the photoanode/electrolyte interface (R_2, second semicircle in the plot). The values of R_S', R_1 and R_2 are calculated to

be 11.20 Ω, 4.85 Ω, and 22.70 Ω for the ATO DSSC and 13.33 Ω, 4.35 Ω and 48.51 Ω for the ATO-H DSSC respectively. Thus R_2 mainly contributes to the increased system resistance in ATO-H based device. It is known that the electrical conductivity (σ) can be expressed by $\sigma = ne\mu$, where n is the electron concentration, e the elementary charge, and μ the electron mobility. In our previous report, slightly doped ATO nanotubes have been achieved via electrochemical process, which delivered increased conductivity and improved power conversion efficiency as well.[18] While in terms of plasma-assisted doping process, the large amount of oxygen vacancy-Ti^{3+} defects and the increased electrical conductivity (σ) were demonstrated in detail.[15] Thus, even though the electrical conductivity (σ) and electron concentration (n) are increased, the electrical mobility (μ) is decreased. During the energy conversion process in the DSSC, the oxygen vacancy-Ti^{3+} defects decrease the electron mobility and serve as recombination centers, which is responsible to the increased R_2 and poor power conversion efficiency.[13]

2.2.2. SC Based on TiO_2 Arrays on Ti Foil with Plasma-Assisted Hydrogenation

On the contrary, plasma-assisted hydrogenation has been demonstrated as an efficient approach to enhance the capacitance of ATO electrodes in our previous work.[15] It is known that the carriers are driven by the built-in voltage in DSSCs, which is determined by the energy difference between the work function of the electrode material and the redox potential of the electrolyte. The increased trap states play a dominant role compared to the increased carrier concentration and as a result hinder effective charge collection. While the electrons are driven by an external field in SCs, which could diminishe the unexpected recombination. In addition, the increased specific surface area and hydrogen passivation of disordered states also contribute the improved electrochemical performance.[15] Herein, the electrochemical performance of the SCs based on ATO and ATO-H electrodes are characterized in a symmetric two-electrode configuration. Cyclic voltammogram (CV) curves at the scan rate of 100 mV/s for both SCs are recorded in **Figure 3**a. The larger integrated area indicates the better capacitive characteristics of ATO-H based SC. The areal capacitance for each device was evaluated by the galvanostatic charge/discharge test at the current density of 1 mA/cm^2 (Figure 3b), which was calculated to be 0.215 mF/cm^2 for ATO SC and 1.100 mF/cm^2 for ATO-H SC respectively. According to our previous work, the much increased charge storage capacity is ascribed to two factors: the highly rough surface induced by the plasma etching effects and the large amounts of oxygen-Ti^{3+} vacancies serving as active sites in the amorphous layer.[15]

Figure 3c shows the CV curves for ATO-H SC at different scan rates over the wide range from 0.01 to 1 V/s. Even at the extremly high scan rates of 10 V/s (inset of Figure 3c), the curve still presents quasi-rectangular shape, manifesting the excellent rate capability. The galvanostatic charge/discharge measurements for ATO-H SC are also conducted with current densities varied from 0.1 to 2 mA/cm^2 with 0.63 V voltage window to calculate the specific capacitance of the ATO-H SC (Figure 3d). An areal capacitance of 1.072 mF/cm^2 is obtained at the current density of 0.1 mA/cm^2. Electrochemical impedance spectroscopy (EIS) is an efficient tool to evaluate the electrochemical performance of supercapcacitors. Figure 3e exhibits the Nyquist plot for ATO-H SC in the frequency range from 0.01 to 100 kHz.

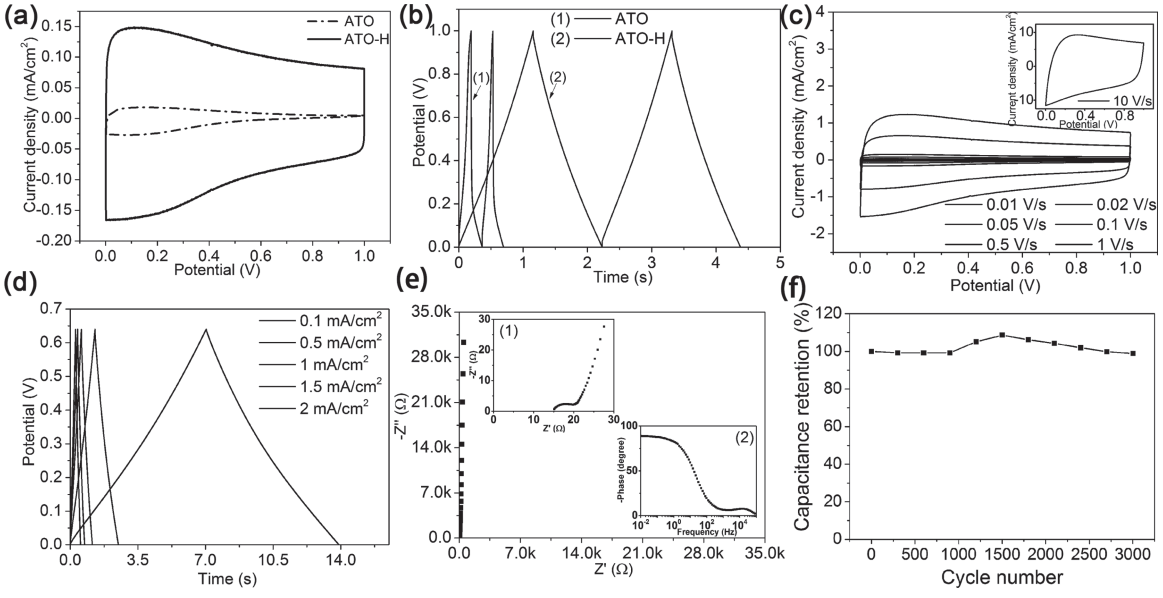

Figure 3. (a) CV curves of ATO and ATO-H SCs at the scan rate of 100 mV/s. (b) Galvanostatic charge/discharge curves at the current density of 1 mA/cm^2 for ATO and ATO-H SCs with the voltage window of 1 V, respectively. (c) CV curves of the ATO-H SC recorded at the scan rate from 0.01 to 10 V/s respectively.(d) Galvanostatic charge/discharge curves of the ATO-H SC at different current densities with the voltage window of 0.63 V. (e) Electrochemical impedance spectra of the ATO-H SC in the frequency range of 0.01–100 kHz. Inset (1) shows the large view of the Nyquist plot at the high-frequency region. Inset (2) shows the Bode plot of the device. (f) The capacitance stability of the ATO-H SC measured by the galvanostatic charge/discharge test for 3000 cycles.

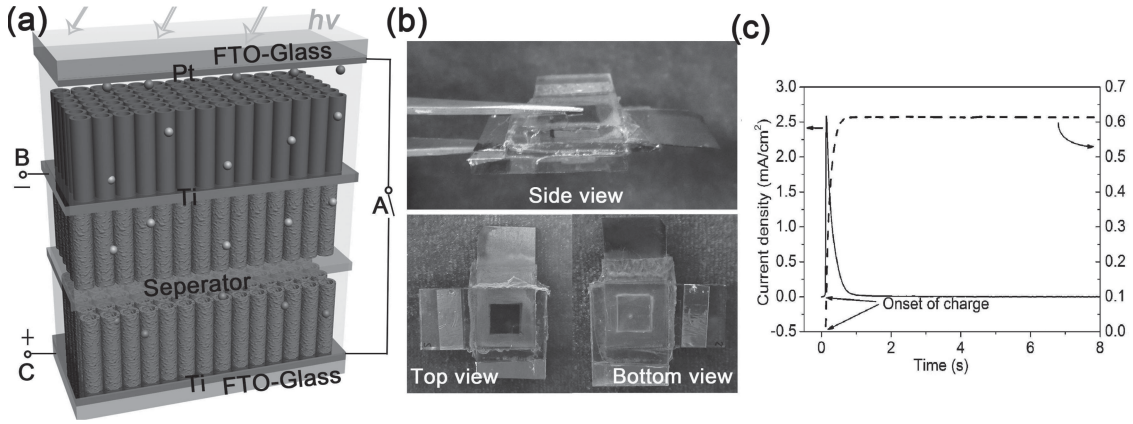

Figure 4. (a) Structure schematic illustration and work mechanism of the PSC. (Dark-gray balls represent positive charges and light-gray balls represent electrons). (b) The side, top (DSSC part) and bottom view (SC part) of the as-fabricated PSC device. (c) The current density and voltage transients of SC during photocharge.

The expanded view of the semicircle in the high frequency range is shown in inset (1). The intercepts of Nyquist plots on the real axis is about 15 Ω, representing the conductivity of the electrolyte (R_s). The extremely small semicircle diameter indicates low charge transfer resistance of the electrode. In inset (2), the phase angle of the capacitor reached –89.1° at the frequency of 0.01 Hz, approaching to the ideal capacitor characteristics with the phase angle of –90° approximately. In the low frequency region, the capacitor response frequencies at the phase angle of –45° is recorded to be 21.5 Hz. Thus the relaxation time constant (τ_o) was calculated to be 46.5 ms by the equation of $\tau_o = 1/f_o$, which is much faster than 6.67 s for the activated carbon capacitors and even comparable with 33.3 ms for the graphene based capacitors.[22] The ATO-H based SC presents capacitance retention with ratio exceeding 100% of initial capacitance after 1000 cycles at the current density of 1 mA/cm^2 (Figure 3f). This behavior probably originates from self-activation process of electrode, namely the initial cycles allow sufficient absorption and intercalation/deintercalation of ions, which generates increased active sites and in turn the enhanced specific capacitance.[23] After 3000 charge/discharge cycles, the capacitance still remains at 98.8% of initial value, manifesting the superior stability of ATO-H electrodes.

2.2.3. Integrated Photo-supercapacitor Based on Bi-polar TiO_2 Nanotube Arrays with Selective One-Side Plasma-Assisted Hydrogenation

Due to the simultaneously formed nanotubes on both sides of Ti foil, it is possible to assemble the DSSC and SC into a light charged PSC. According to above results, selective one-side hydrogenation, forming ATO/Ti/ATO-H architecture, is highly desired to optimize the integrated device. **Figure 4**a illustrates the configuration of integrated PSC. Switch A is readily to be turned on to trigger the photo-charge process. The corresponding photograph from side, top and bottom views are shown in Figure 4b, presenting a three-electrode system with a sandwich structure. During the photo-charge process, the photo-excited electrons collected from dye molecules are transferred from the conduction band of the pristine ATO to the other side with hydrogenated nanotubes. Figure 4c depicts the real-time response of photo-voltage and photo-current density of the PSC. On visible light illumination, a pulsed anodic photocurrent around 2.6 mA/cm^2 occurred promptly and then gradually decayed to 0.025 mA/cm^2 in 1 s. Consequently, a maximum and stable charge voltage of 0.61 V is achieved on SC after being photo-charged for 1 s, approaching to the open-circuit voltage of the DSSC (0.63 V).

Figure 5a exhibits the photocharge and galvanostatic discharge process of the PSC at different discharge current densities from 0.1 mA/cm^2 to 2 mA/cm^2. To keep the system stable, the charge process was maintained for 10 s consistently. Interestingly, the discharge times of the PSC are a little bit longer than those of pure SC (Figure 3d). For comparison, the calculated areal capacitances of the PSC and SC versus the discharge current densities are plotted in Figure 5b. The self-discharge measurements were also applied for figuring out the reasons, as shown in Figure 5c. It is observed that the output voltage of the PSC degraded slower than that of the SC, which is in tightly connection with the phenomenon shown in Figure 5b. In these charge/discharge measurements, PSC and SC tests are conducted on the same ATO-H electrodes. The only difference of both measurements is that SC works under dark condition while PSC is evaluated under light illumination. Thus the slightly deviation could be originated from the introduced DSSC sub-device.

In the photocharge process, the final work potential of the DSSC was tested to be 0.61 V according to the maximum output voltage of the PSC, suggesting that a small current is charging to the SC to compensate for the self-discharged loss, as shown in Figure 5d.[7] While in the discharge process with switch A shut down under continuous illumination, the DSSC recovered to the open-circuit state (0.63 V). Under this condition, some extra electrons will be accumulated on the photoanode, leading to a tiny negative current to the negative electrode of the SC part (Figure 5e). However, the delay effect of the voltage transient would not happen in conventional charge process, as illustrated in Figure 5f,g.

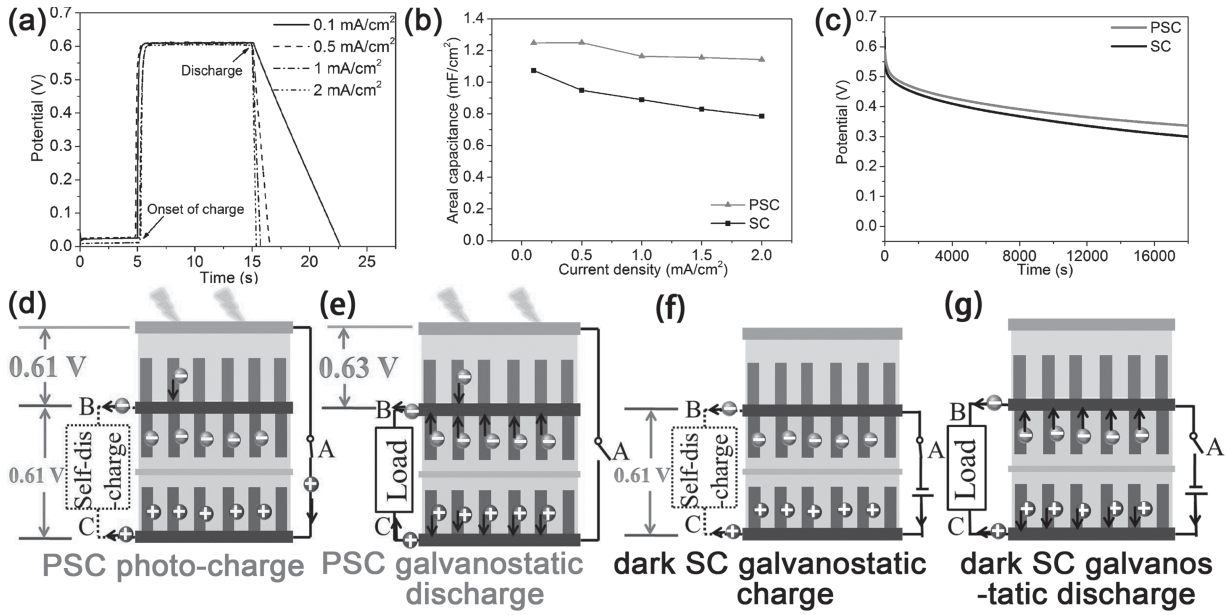

Figure 5. (a) The photocharge/galvanostatic discharge curves of the PSC at different current densities. (b) The areal capacitance for the PSC and the SC part charged by the electrochemical work station plotted vs. current density respectively. (c) The self-discharge curves of the PSC and the pure SC part charged by the electrochemical work station as a function of time. (d) The mechanism illustration of the steady state of the PSC after being fully photocharged. (e) The discharge process of PSC. (f) The mechanism illustration of the steady state of the SC after being fully charged by external power source. (g) The discharge process of SC.

The cycle stability of the PSC is also investigated for 100 cycles at a discharge current density of 0.1 mA/cm^2 (**Figure 6**a) and the curve of first 5 cycles are displayed in the inset. The discharge areal capacitance retained up to 96.5% of its initial capacity (1.289 mF/cm^2), indicating the superior stability of the PSC device. The energy density of the PSC (E_{PSC}) was calculated to be 6.662 × 10^{-8} Wh/cm^2 according to the Equation 3 in the experiment section. Within the first second of photocharge shown in Figure 4c, the overall photoelectric conversion and storage efficiency curve versus photocharge time is calculated based on Equations (3), (5) and (6) (Note: the $C_{(PSC)A}$ is 1.289 mF/cm^2, ΔV is the measured values in the V–t curve in Figure 4c), as shown in Figure 6b.[8] Thus the integrated PSC device yields maximum overall photoelectric conversion and storage efficiency ($\eta_{overall}$) and maximum energy storage efficiency ($\eta_{storage}$) up to 1.64% (Figure 6b) and 51.60%, respectively. It is worth noting that the photo-charge is a dynamic process. Equation (7) has simplified the system by assuming the charge process carried out under the maximum output energy density of DSSC, i.e., the calculated η_{DSSC}. Thus the real energy storage efficiency ($\eta_{storage}$) is generally below η_{PSC}. In this sense, smart power-conversion techniques are desirable to be introduced into this integrated device, which will extract more power from solar cells to energy storage devices.

Given the practical application of the PSC, a tandem system based on 4 individual devices is demonstrated. In the photo-charge process, the DSSC parts and SC parts are connected in series as illustrated in **Figure 7**a. In the discharge process, DSSC sub-devices are disconnected while keep SCs working (Figure 7b). The photograph of the tandem PSC system is shown in Figure 7c. The discharging profiles from a stable output voltage of 2.5 V under different current densities are recorded in Figure 7d. A discharge

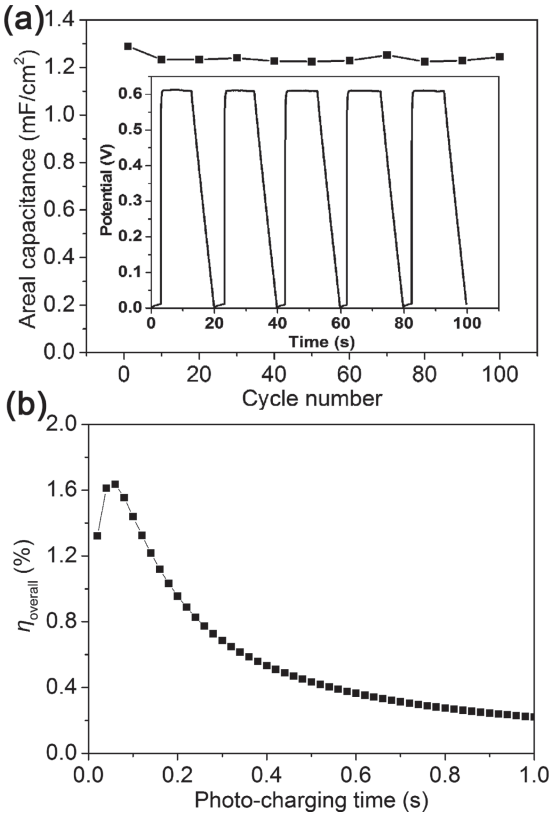

Figure 6. (a) Photocharge/galvanostatic discharge cycle stability of the PSC device (inset shows the output voltage-time curves of first five cycles). (b) The overall photoelectric conversion and storage efficiency ($\eta_{overall}$) of the PSC versus the photocharge time.

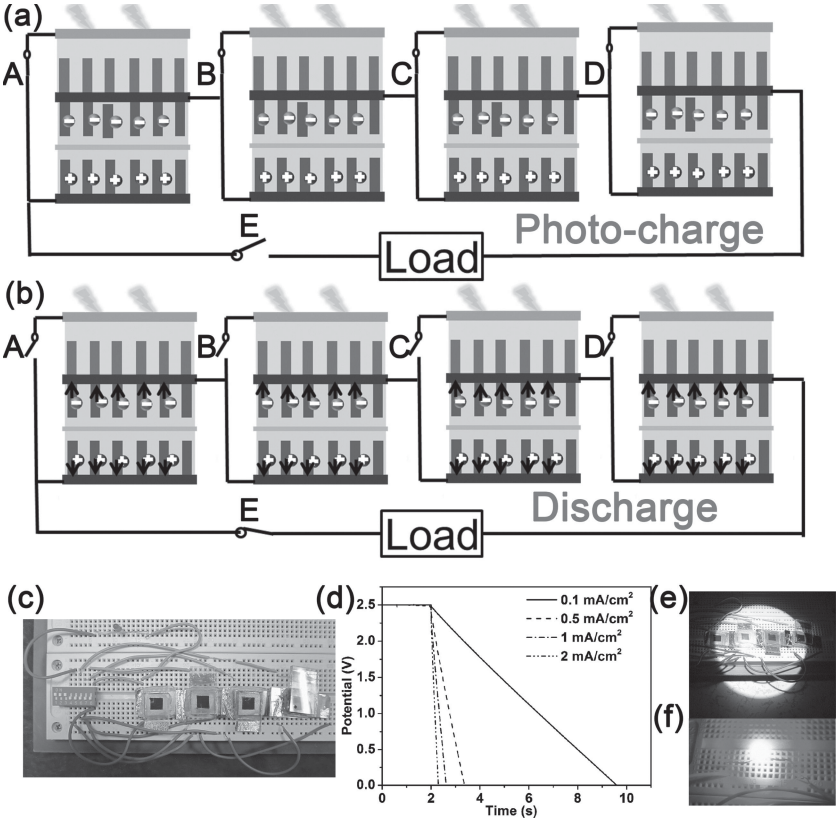

Figure 7. (a) The electric-circuit schematic illustration of the tandem PSC system for photocharge process and the discharge process respectively. (c) The photograph of the tandem PSC system. (d) The galvanostatic discharge curves of the PSC tandem system at different current densities after being photocharged. (e) The photograph of the photocharge process. (f) The energy stored in the tandem PSC system was used to drive a red LED.

current density of 0.1 mA/cm^2 yields an overall areal capacitance of 0.304 mF/cm^2, following the principle of capacitors in series connection. Subsequently, the as assembled device arrays are used to drive a LED after being photo-charged for 10 s (as shown Figure 7e,f). This result demonstrates the feasibility of the fabricated PSC system in integrated energy conversion and energy storage.

3. Conclusions

An integrated PSC based on bi-polar ATO nanotube arrays with selectively hydrogen plasma treatment on SC sub-device was successfully developed. Taking advantage of the simultaneously optimized DSSC and SC sub-devices, the PSC presents a maximum energy storage efficiency of 51.60% and an remarkable overall photoelectric conversion and storage efficiency up to 1.64% with fast response and superior cycling capability. In contrast to traditional power conversion and storage system, the novel PSC successfully delivers the light-weight, facile-fabricating, and energy-saving characteristics. By improving the fabrication and packaging technique, the integrated PSC will boost the development of solar-driven system, responding to the calls for energy conservation and emission reduction.

4. Experimental Section

Fabrication of ATO and ATO-H: Ti foils (0.2 mm thickness) are cleaned by acetone, ethanol and distilled water firstly following an annealing process (450 °C for 2 h). Self-organized ATO nanotube films (2 cm × 2 cm) are prepared by two-step anodization of the Ti foils in ethylene glycol electrolyte containing NH_4F (0.5 wt%) and H_2O (2 vol%) as described in our previous literatures.[15] Typically, first-step anodization is performed at 60 V for 2 h in a conventional two-electrode configuration with a carbon rod as cathode electrode. The as-obtained nanotube films are removed from the Ti foil with adhesive tape. The second-step anodization is performed under the same conditions as the first process. Finally, the as-prepared TiO_2 nanotubes were annealed at 150 °C for 2h, then up to 450 °C for 3h. The crystallized TiO_2 nanotube films, denoted as ATO, are used for the subsequent plasma treatments. For the preparation of hydrogenated ATO (denoted as ATO-H), the ATO nanotube films are loaded into the processing chamber of plasma-enhance chemical vapor deposition plasma enhanced chemical vapor deposition (PECVD) system and preheated in vacuum at 320 °C for 30 min before plasma illumination. Hydrogen plasma is then induced with a radio-frequency power source (13.56 MHz, 40 W) along with hydrogen gas flow at 100 sccm under 50 Pa. The hydrogenation treatment is set as 1.5 h followed by 1 h cooling down before taking the sample out. Consequently, the bi-polar ATO-H with hydrogen dope on one side is fabricated, which appears to be blue on the hydrogenated side instead of white.

Assembly of Supercapacitor (SC) Part: The supercapacitor part of the integrated device is assembled on the hydrogenated side of the ATO-H. Firstly, a piece of glass fiber separator (size: 0.6 cm × 0.6 cm) is sandwiched between the bi-polar ATO-H electrode (active material area: 0.5 cm × 0.5 cm) and a single-polar ATO-H (electrode size: 0.5 cm × 0.5 cm). Then, a FTO glass with a hole in the center is attached to the Ti foil of single-polar ATO-H to assemble both electrodes together, sealing with surlyn (Dupont) at 120 °C on the hot plate. Electrolyte of Li_2SO_4 (2 M) solution is injected through the hole, which is sealed with a cover glass finally.

Assembly of Dye-Sensitized Solar Cell (DSSC) Part: After the fabrication of the SC part, the untreated side of ATO-H is employed as the photoanode of DSSC, which is sensitized by cis-bis(isothiocyanato) bis(2,2-bipyridyl-4,4-dicarboxylato) ruthenium(II)bis-tetrabutylammonium dye (N-749) solution in ethanol (0.5 mM) for 24 h. The dried photoelectrode is sandwiched against a Pt counter-electrode filled with electrolyte consisting of DMPII (1.0 M), LiI (0.1 M), I_2 (0.12 M), and 4-TBP (0.5 M) in methoxypropionitrile to assemble typical DSSCs.

Characterization and Measurement: The morphology and crystal structure of as-obtained samples are characterized by field emission scanning electron microscopy (FESEM, Sirion 200), high resolution transmission electron microscopy (HRTEM). X-ray diffraction patterns (XRD) were obtained from an X-ray diffractometer (D8 ADVANCE, Bruker AXS, Germany) with radiation of a Cu target (Ka, λ = 0.15406 nm). Photocurrent-voltage measurements of DSSC are done under simulated solar illumination (100 mW/cm^2) from a Xe lamp coupled with an AM 1.5G filter (Newport No. 94063A). The electrochemical impedance spectra of DSSC (–0.7V, 100 kHz-0.01 Hz, 5 mV amplitude), CV, galvanostatic charge/discharge measurements, electrochemical impedance spectroscopy (0V, 100 kHz-0.01 Hz, 5 mV amplitude) and cycling performance of SCs are collected by a CHI 760D, with automatic data acquisition. The modeled equivalent circuit was simulated by the Zsimpwin software.

Calculations: The capacitance (C) and areal capacitance (C_A) of the SC and the PSC are calculated from the galvanostatic discharge curves at different current densities using the formula respectively:[22]

$$C = i/(-dV/dt) \quad (1)$$

$$C_A = C/A_{SC} \quad (2)$$

where i (in amps, A) is the applied current, and dV/dt the slope of the discharge curve (in volts per second, V/s). Specific capacitances were calculated based on the area of the device stack, where A_{SC} refers to the area (0.25 cm^2) of the SC.

The areal energy density (E_{PSC}) of the PSC derived from photo-charge/galvanostatic discharge curves are calculated from the following expression:[22]

$$E_{PSC} = 0.5C_{(PSC)A}(\Delta V)^2 \quad (3)$$

where ΔV is the operating voltage window (measured in volts and obtained from the discharge curve excluding the voltage drop) and $C_{(PSC)A}$ is the areal capacitance of the PSC.

The energy-conversion efficiency ($\eta_{conversion}$) of the PSC derived from the DSSC *I-V* curves and the illuminating light energy on the DSSC (E_{light}) per unit area are calculated using the following expression:

$$\eta_{conversion} = FFV_{OC}J_{SC}/P_{in} \quad (4)$$

$$E_{light} = P_{in} \times t \quad (5)$$

where FF, V_{OC}, J_{SC}, and P_{in} correspond to fill factor, open-circuit voltage, short-circuit current density, and incident light power density (100 mW/cm^{-2}), respectively. t refers to the photo-charging time of the PSC.

The overall photoelectric conversion and storage efficiency of the PSC ($\eta_{overall}$) is calculated as follows:[8]

$$\eta_{overall} = E_{PSC} \times A_{PSC}/E_{light} \times A_{DSSC} \quad (6)$$

A_{PSC} and A_{DSSC} are the effective area (0.25 cm^2) of the SC and DSSC part of the PSC device, respectively.

The energy-storage efficiency ($\eta_{storage}$) in the energy-storage part of the PSC is calculated based on following formula:

$$\eta_{storage} = \eta_{overall}/\eta_{conversion} \quad (7)$$

Acknowledgements

This work was supported by the National Natural Science Foundation of China (21001046, 51102271, 91123008, 61377033), the 973 Program of China (2011CB933300), the Program for New Century Excellent Talents of the University in China (No. NCET-11–0179), the Natural Science Foundation of Shanghai (11ZR1436300), Shanghai Rising-Star Program(11QA1406400), and Shanghai Municipal Human Resources and Social Security Bureau (2011033).

Received: August 30, 2013
Revised: October 6, 2013
Published online: November 18, 2013

[1] J. Burschka, N. Pellet, S.-J. Moon, R. Humphry-Baker, P. Gao, M. K. Nazeeruddin, M. Grätzel, *Nature* **2013**, *499*, 316.
[2] J. R. Miller, P. Simon, *Science* **2008**, *321*, 651.
[3] R. P. Raffaelle, J. Underwood, D. Scheiman, J. Cowen, P. Jenkins, A. F. Hepp, J. Harris, D. M. Wilt, 20th *IEEE PVSC* **2000**, 1370.
[4] H. Nagai, H. Segawa, *Chem. Commun.* **2004**, 974.
[5] A. Hauch, A. Georg, U. O. Krašovec, B. Orel, *J. Electrochem. Soc.* **2002**, *149*, A1208.
[6] W. Guo, X. Xue, S. Wang, C. Lin, Z. L. Wang, *Nano Lett.* **2012**, *12*, 2520.
[7] T. Chen, L. Qiu, Z. Yang, Z. Cai, J. Ren, H. Li, H. Lin, X. Sun, H. Peng, *Angew. Chem. Int. Ed.* **2012**, *51*, 11977.
[8] Y. Fu, H. Wu, S. Ye, X. Cai, X. Yu, S. Hou, H. Kafafy, D. Zou, *Energy Environ. Sci.* **2013**, *6*, 805.
[9] T. Chen, Z. Yang, H. Peng, *ChemPhysChem* **2013**, *14*, 1777.
[10] X. Xia, J. Luo, Z. Zeng, C. Guan, Y. Zhang, J. Tu, H. Zhang, H. J. Fan, *Sci. Rep.* 2012, DOI: 10.1038/srep00981.
[11] G. Wee, T. Salim, Y. M. Lam, S. G. Mhaisalkar, M. Srinivasan, *Energy Environ. Sci.* **2011**, *4*, 413.
[12] Y. Xie, N. Huang, S. You, Y. Liu, B. Sebo, L. Liang, X. Fang, W. Liu, S. Guo, X.-Z. Zhao, *J. Power Sources* **2013**, *224*, 168.
[13] Y. Yu, K. Wu, D. Wang, *Appl. Phys. Lett.* **2011**, *99*, 192104.
[14] X. Lu, G. Wang, T. Zhai, M. Yu, J. Gan, Y. Tong, Y. Li, *Nano Lett.* **2012**, *12*, 1690.
[15] H. Wu, C. Xu, J. Xu, J. Wang, B. Yang, H. Huang, L. Lu, D. Liu, Z. Fan, P. Chang, X. Zhu, X. Chen, Y. Song, D. Li, *Nanotechnology* **2013,** *24*, 455401.
[16] R. P. H. Chang, C. C. Chang, S. Darack, *J. Vac. Sci. Technol.* **1982**, *20*, 490.
[17] J. Zhu, S. Wang, Z. Bian, S. Xie, C. Cai, J. Wang, H. Yang, H. Li, *CrystEngComm* **2010**, *12*, 2219.
[18] D. Li, P.-C. Chang, C.-J. Chien, J. G. Lu, *Chem. Mater.* **2010**, *22*, 5707.
[19] Z. Wang, H. Wang, B. Liu, W. Qiu, J. Zhang, S. Ran, H. Huang, J. Xu, H. Han, D. Chen, G. Shen, *ACS Nano* **2011**, *5*, 8412.
[20] Y. H. Jang, X. Xin, M. Byun, Y. J. Jang, Z. Lin, D. H. Kim, *Nano Lett.* **2011**, *12*, 479.
[21] http://www.echemsw.com/prod01.htm, accessed: March, 2013.
[22] M. F. El-Kady, V. Strong, S. Dubin, R. B. Kaner, *Science* **2012**, *335*, 1326.
[23] X. Lu, G. Wang, T. Zhai, M. Yu, S. Xie, Y. Ling, C. Liang, Y. Tong, Y. Li, *Nano Lett.* **2012**, *12*, 5376.